PHYSICAL REVIEW B **97**, 125203 (2018)

Spin-to-charge conversion for hot photoexcited electrons in germanium

C. Zucchetti,[1,*] F. Bottegoni,[1] G. Isella,[1] M. Finazzi,[1] F. Rortais,[2] C. Vergnaud,[2] J. Widiez,[3] M. Jamet,[2] and F. Ciccacci[1]
[1]*LNESS, Dipartimento di Fisica, Politecnico di Milano, Piazza Leonardo da Vinci 32, 20133 Milan, Italy*
[2]*Université Grenoble Alpes, CEA, CNRS, Grenoble INP, INAC-Spintec, 38000 Grenoble, France*
[3]*Université Grenoble Alpes, CEA, LETI, DCOS, LIFT, F-38000 Grenoble, France*

(Received 13 December 2017; revised manuscript received 6 February 2018; published 19 March 2018)

We investigate the spin-to-charge conversion in highly doped germanium as a function of the kinetic energy of the carriers. Spin-polarized electrons are optically generated in the Ge conduction band, and their kinetic energy is varied by changing the photon energy in the 0.7–2.2 eV range. The spin detection scheme relies on spin-dependent scattering inside Ge, which yields an inverse spin-Hall electromotive force. The detected signal shows a sign inversion for $h\nu \approx 1$ eV which can be related to an interplay between the spin relaxation of high-energy electrons photoexcited from the heavy-hole and light-hole bands and that of low-energy electrons promoted from the split-off band. The inferred spin-Hall angle increases by about 3 orders of magnitude within the analyzed photon energy range. Since, for increasing photon energies, the phonon contribution to spin scattering exceeds that of impurities, our result indicates that the spin-to-charge conversion mediated by phonons is much more efficient than the one mediated by impurities.

DOI: 10.1103/PhysRevB.97.125203

I. INTRODUCTION

Spintronics aims at the active control of the carriers' spin degree of freedom to implement new functionalities in electronic devices [1–3]. Although semiconductors do not possess a spin-polarized carrier population at equilibrium, net spin densities can be generated either by doping with dilute magnetic impurities [3–5] or with electrical [2,6,7], mechanical [8], and optical [9–13] injection of angular momentum. Moreover, spintronics can also exploit spin-to-charge and charge-to-spin conversion phenomena [such as spin-Hall (SHE) and inverse spin-Hall (ISHE) effects], as shown in GaAs [14–17] and more recently in Ge [18–21] and Si [22].

Another important issue of spintronics consists of understanding the spin dynamics of the carriers injected into a semiconductor. In this respect, among all the generation techniques, optical orientation is particularly interesting since the initial energy distribution of the photoexcited carriers can be tuned by selecting the wavelength of the impinging photons [10]. Both Ge and GaAs allow efficient optical spin injection, thanks to the high spin-orbit interaction, which, at Γ, separates the heavy-hole (HH) and light-hole (LH) bands from the split-off (SO) one by a large energy Δ_0. This allows reaching a photoelectron spin polarization P in the conduction band (CB) immediately after photon absorption up to 50% for a wide range of photon energies above the direct gap E_{dg}, with $P = (n_\uparrow - n_\downarrow)/(n_\uparrow + n_\downarrow)$, where $n_{\uparrow(\downarrow)}$ is the spin-up (-down) density referred to a quantization axis parallel to the light wave vector [10,23,24].

In this work, we focus our attention on Ge, which is characterized by a much larger spin diffusion length than GaAs, opening the possibility of designing multiterminal spintronic devices which are inaccessible to a GaAs-based platform [18,25]. This is due to the fact that the efficient Dyakonov-Perel spin-depolarization channel [4,26–28] is active only in a noncentrosymmetric lattice such as that of GaAs and is therefore totally suppressed in Ge. Moreover, Ge represents the most natural choice for the integration of spintronics, photonics, and electronics functionalities on a platform compatible with currently employed technologies. In fact, on the one hand, the Ge direct gap matches the 1550-nm telecommunication wavelength [29,30], and on the other hand, the 4% lattice mismatch with Si allows for the ready integration of Ge with a Si-based platform and for the growth of strain-engineered SiGe heterostructures [13].

In this paper we study the spin-to-charge conversion at room temperature in highly n and p doped Ge on insulating substrates fabricated using the germanium-on-insulator (GOI) technique. The spin-polarized electrons are generated by optical orientation directly in Ge. The spin current $\mathbf{j}_{\mathrm{s}}$ resulting from spin diffusion undergoes spin-dependent scattering, known as the inverse spin-Hall effect, which gives rise to a carrier current $\mathbf{j}_{\mathrm{c}}$ normal to both $\mathbf{j}_{\mathrm{s}}$ and the spin-polarization unit vector $\mathbf{u}_P$ [31]:

$$\mathbf{j}_{\mathrm{c}} = \gamma\, \mathbf{j}_{\mathrm{s}} \times \mathbf{u}_P, \tag{1}$$

where γ is the spin-Hall angle, which expresses the efficiency of spin-to-charge conversion. Thus, in open-circuit conditions, the spin current generates an electric voltage ΔV_{ISHE} measured between two Ohmic contacts at the edges of the Ge stripes. The detected signal is analyzed as a function of the incoming photon energy $h\nu$ and is found to reverse sign around $h\nu \approx 1$ eV. Such a result can be understood in the frame of a model that explicitly accounts for momentum, energy, and spin relaxation of optically excited carriers. Within this model, we investigate the dependence of the spin-Hall angle γ of Ge as a function of the incoming photon energy. We report an increase of γ up

---

[*] carlo.zucchetti@polimi.it

2469-9950/2018/97(12)/125203(7)

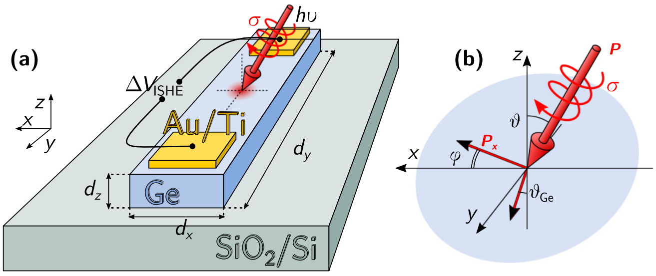

FIG. 1. (a) Sketch of the sample. A single crystalline Ge stripe of dimensions $d_x \times d_y \times d_z = 1 \times 20 \times 1\,\mu\mathrm{m}^3$ lies on top of SiO_2/Si. Two Au/Ti pads deposited onto the stripe allow measuring the photoinduced ISHE signal ΔV_{ISHE}. (b) Experimental geometry: ϑ and φ are the polar and azimuthal angles of the incident light, respectively.

to 0.1 with the photon energy. This value is much larger than the ones reported up to now for semiconductors ($\gamma < 0.02$) [18,32–36]. In the following, we will show that this trend indicates a higher efficiency of spin-to-charge conversion by phonon scattering as compared to impurity scattering.

Momentum, energy, and spin relaxation have been shown to play a relevant role in determining the degree of circular polarization of photoluminescence from both the direct [37] and indirect [38] gaps of Ge. However, photoluminescence probes only the electrons undergoing radiative recombination from the bottom of Γ or L valleys, whereas ISHE is sensitive also to the spin currents generated by nonrelaxed electrons.

II. METHODS

The GOI wafer was fabricated by employing the Smart Cut process [39]. The resulting GOI substrate consisted of 1-μm-thick Ge layers on top of a 1-μm-thick buried oxide. To study spin transport in well-defined conducting channels, Ge films were in depth implanted with either phosphorus for n type ($2 \times 10^{19}\,\mathrm{cm}^{-3}$, resistivity $\rho_n = 1.2\,\mathrm{m}\Omega\,\mathrm{cm}$) or boron for p type ($5 \times 10^{18}\,\mathrm{cm}^{-3}$, resistivity $\rho_p = 3.9\,\mathrm{m}\Omega\,\mathrm{cm}$), exploiting multiple ion implantations at different energies in order to obtain a uniform doping all along the film thickness of 1 μm. The Ge layer was protected against oxidation by a 10-nm-thick SiO_2 film, which was removed using hydrofluoric acid before the introduction into the evaporation chamber to deposit the Au(150 nm)/Ti(10 nm) Ohmic contacts. Then, the samples were processed by optical lithography and reactive ion etching to obtain the geometry of Fig. 1(a). The dimensions of the stripes along the x,y, and z axes [see Fig. 1(a)] are $d_x \times d_y \times d_z = 1 \times 20 \times 1\,\mu\mathrm{m}^3$, respectively.

Optical orientation is performed as indicated in Fig. 1 [10,17]. As a tunable light source, we use the monochromatized light (typical bandwidth of 10 meV) from a supercontinuum laser delivering nanosecond pulses at a 78-MHz repetition rate in the 0.7–2.2 eV range [40]. In our geometry, as reported in Refs. [15,17,22], the detectable $\mathbf{j}_s$ current density is parallel to the z axis. Since the Ohmic contacts detect a $\mathbf{j}_c$ current density directed along y, the measured ΔV_{ISHE} is sensitive only to the x component of $\mathbf{P} = P\mathbf{u}_P$ [see Eq. (1)]. To obtain a significant in-plane component of the polarization, the laser beam partially fills off axis a 0.65 numerical aperture objective, focusing the light on the sample with a polar angle $\vartheta \approx 20^\circ$ [see Fig. 1(b)] [41], thus producing a polar angle ϑ_{Ge} inside the Ge layer that is between 3.3° and 4.7°, within the analyzed photon energy range. All the measurements were performed at room temperature.

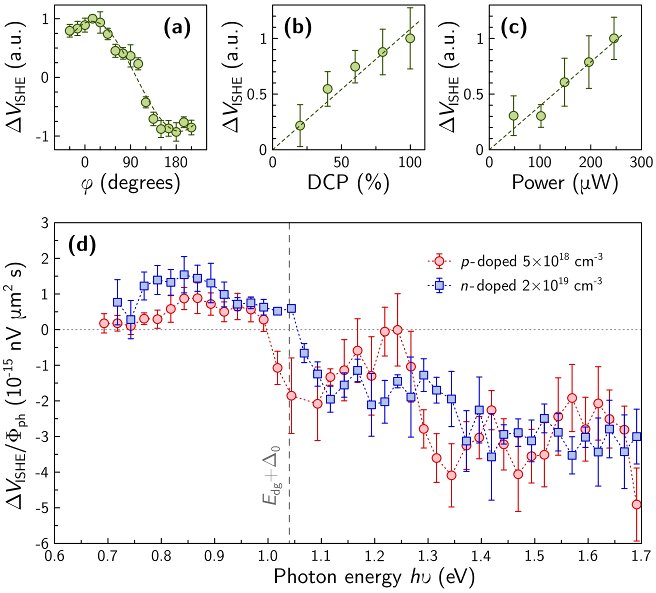

FIG. 2. ISHE signal measured in the n-doped sample ($h\nu = 1.97\,\mathrm{eV}$) as a function of (a) φ [see Fig. 1(b)], with optical power absorbed by Ge $W = 246\,\mu\mathrm{W}$ and degree of circular polarization DCP = 100%; (b) DCP, with $W = 246\,\mu\mathrm{W}$ and $\varphi = 0^\circ$; and (c) W for DCP = 100% and $\varphi = 0^\circ$. (d) ISHE signal in p-doped (red circles) and n-doped (blue squares) samples as a function of the incident photon energy. Each data point represents the average value of ten acquisitions with an integration time of 200 s. The bars account for the fluctuations of the data to twice their standard deviation. The vertical gray dashed line marks the onset of SO transitions, $h\nu = E_{\mathrm{dg}} + \Delta_0 = 1.04\,\mathrm{eV}$.

The ISHE signal is measured with a lock-in amplifier by modulating the light circular polarization with a photoelastic modulator (PEM) operating at 50 kHz [15,17]. To further increase the signal-to-noise ratio, the light intensity was modulated by a chopper at 21 Hz, and the signal was extracted by a second lock-in amplifier in cascade with the first.

III. RESULTS AND DISCUSSION

A. ISHE data

The spin-related nature of the detected signal is confirmed by the data sets in Figs. 2(a)–2(c). Figure 2(a) reports the dependence of ΔV_{ISHE} as a function of φ [defined in Fig. 1(b)], which follows the cos(φ) geometrical dependence expected from Eq. (1) [15,17,22,42]. The proportionalities of ΔV_{ISHE} with the degree of circular polarization (DCP) of the incident light and with the absorbed light power W are shown in Figs. 2(b) and 2(c), respectively [21,22].

The dependence of ΔV_{ISHE} normalized to the photon flux $\Phi_{\mathrm{ph}} = W/[\pi(d/2)^2\,h\nu]$, with d being the diameter of the laser spot, is reported in Fig. 2(d) as a function of the incident photon energy in the 0.7–1.7 eV range for n-doped (blue squares) and p-doped samples (red circles). For both analyzed samples,

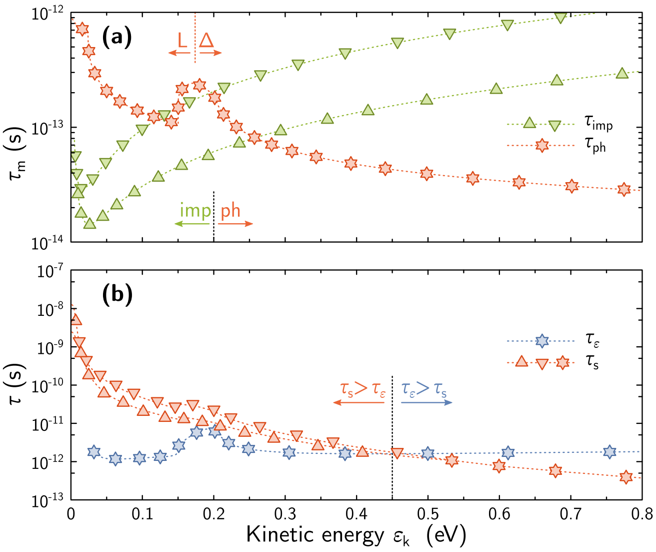

FIG. 3. Relaxation times of spin-polarized electrons in Ge (for further information see Sec. III B and the appendices). Triangles pointing upwards (downwards) refer to *n*- (*p*-) doped samples, and stars refer to both. The vertical lines separate different regimes, as discussed in the text. (a) Impurity (green) and phonon (red) momentum relaxation times. (b) Energy (blue) and spin (red) lifetimes.

the signal reverses sign at $h\nu \approx E_{dg} + \Delta_0 \approx 1.04$ eV, which corresponds to the onset of excitations from the SO band [43]. Note also that the measured signal increases by roughly a factor 3 at the highest photon energy investigated.

As will be shown in the following, the sign reversal originates from the dependence of relaxation times versus the photoelectron kinetic energy, addressed in Sec. III B. Indeed, as stated in Eq. (1) the interpretation of the data is based on the knowledge of the spin current density $\mathbf{j}_s$, which depends on the spin-relaxation time and the spin polarization at the generation time, as analyzed in Secs. III C and III D. Notice that, although our data are not time resolved, we introduce a model that explicitly accounts for the temporal dependence of the spin polarization. This is necessary in order to correctly reproduce the experimental observations and gain insight into the physical mechanism leading to the observed behavior.

B. Relaxation times

The above experimental results can be rationalized by modeling the momentum, energy, and spin-relaxation processes, which determine the electron spin dynamics. Momentum relaxation is discussed in Appendix A and arises from two main contributions: scattering with impurities (expressed by the impurity-scattering time τ_{imp}) and with phonons (expressed by the phonon-scattering time τ_{ph}). For the latter, we take into account all the inter- and intravalley phonon-scattering mechanisms involving the L, Γ, and Δ valleys. The total momentum relaxation rate ${\tau_m}^{-1}$ is given by ${\tau_m}^{-1} = {\tau_{imp}}^{-1} + {\tau_{ph}}^{-1}$. As shown in Fig. 3(a), impurities play a significant role for both *n*- (green triangles pointing upwards) and *p*-doped samples (green triangles pointing downwards) only for low kinetic energies ($\varepsilon_k \lessapprox 0.2$ eV). As ε_k increases, the carrier-impurity interaction is reduced, and this contribution can be neglected [44]. On the contrary, the scattering rate of the generic ith phonon process ${\tau_{ph,i}}^{-1}$ increases with kinetic energy as $\sqrt{\varepsilon_k}$. The total phonon relaxation time [red stars, Fig. 3(a)] is obtained by weighting all the phonon-scattering mechanisms as described in Appendix B. It turns out that intravalley scattering is negligible, and inter-LL-valley (inter-$\Delta\Delta$-valley) scattering dominates the phonon scattering at low (high) kinetic energies. The crossover between these two regimes occurs around $\varepsilon_k \approx \Delta E_{L\Delta} = 173$ meV, corresponding to the energy gap between L and Δ valleys.

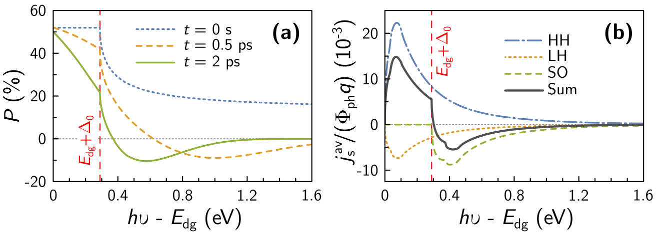

FIG. 4. (a) Spin-polarization spectra at the generation time $t = 0$ (blue dotted line) and after 0.5 ps (orange dashed line) and 2 ps (green solid line). (b) Total average spin current density (gray solid line) and partial contributions originated by electrons excited from the HH (blue dash-dotted line), LH (orange dotted line), and SO (green dashed line) bands. The vertical dashed red line highlights the onset of transitions from SO states.

Basically, impurity scattering is an elastic process, so it does not contribute to energy relaxation [44]. On the contrary, phonon intervalley scattering is anelastic. With $\hbar\omega_i$ being the phonon energy of the ith scattering process, the corresponding energy relaxation time is $\tau_{\varepsilon,i} \approx \tau_{ph,i}\, \varepsilon_k/\hbar\omega_i$ [44]. The τ_ε value, calculated considering all the phonon-scattering processes, is reported in Fig. 3(b) (blue stars).

In addition to momentum and energy relaxation, each scattering event contributes to a partial spin depolarization [4,45]. The dependence on the electron's kinetic energy is expressed by the Yafet-Elliot cross section: $\tau_s \propto \tau_m/{\varepsilon_k}^2$. The resulting τ_s is shown in Fig. 3(b) (red triangles; for further details see Appendix C).

Notably, unlike τ_ε, τ_s strongly depends on the kinetic energy. The two relaxation times are comparable at $\varepsilon_k \approx 0.45$ eV. This kinetic energy separates two different regimes: a low-energy region in which spin polarization is conserved while energy is relaxed and a high-energy one in which electrons depolarize before thermalization occurs.

C. Spin polarization

In Fig. 4(a) we plot snapshots of the spin-polarization spectra at three different time intervals after optical excitation. The spectrum $P_0(h\nu)$ at the generation time ($t = 0$) has been calculated from the usual matrix elements for the HH → CB, LH → CB, and SO → CB transitions [23], with the joint density of states resulting from a parabolic approximation of the band structure around Γ [46]. The onset of transitions from SO ($h\nu = E_{dg} + \Delta_0$) causes the spin polarization P_0 to drop since opposite net spin populations originate from the (HH + LH)-excited electrons and the SO-excited ones [23].

Each population has its own energy distribution in the CB, which can be found from energy conservation [46]. Thus, photoexcited electrons from different bands will experience, for each photon energy, different spin and energy relaxation times. The temporal dependence of the spin-polarization $P(t)$ has been obtained, for each photon energy, by accounting for the evolution of the three independent populations in the CB originating from HH, LH, and, eventually, SO: $P(t) = [n_\uparrow(t) - n_\downarrow(t)]/[n_\uparrow(0) - n_\downarrow(0)]$.

It should be noticed that the polarization changes sign after a certain time if transitions from SO states are allowed ($h\nu \gtrapprox E_{\mathrm{dg}} + \Delta_0$). Indeed, just after the excitation, the polarization is driven by the HH-originated electrons, which have a higher kinetic energy than the minority electrons coming from SO bands. Thus, according to Fig. 3(b), highly kinetic electrons from HH and LH bands undergo efficient depolarization. Conversely, the depolarization of minority electrons from SO states (which have an opposite spin with respect to the ensemble of HH and LH electrons) is less efficient, eventually leading to a polarization reversal. The spin transport is thus dominated, when present, by the SO-excited electrons, which hold their polarization for a longer time and induce the sign reversal of the ISHE signal displayed in Fig. 2(d). This phenomenon should not be confused with the change in the helicity of the photoluminescence from the Γ valley investigated in Ref. [37]. Indeed, there, photoluminescence helicity reversal was related to the higher probability to scatter out of Γ for HH- and LH-originated electrons compared to the ones excited from the SO band.

Note that the parabolic approximation slightly overestimates P_0 compared to the $\mathbf{k} \cdot \mathbf{p}$ calculations of Ref. [23]. A lower starting value of P_0 would, however, only enhance the polarization reversal effect. Moreover, to confirm the robustness of the model, we notice that the time evolution of P is driven by the ratio between τ_ε and τ_{s}. This is independent of the momentum scattering rate, thus decoupling the results from the uncertainties associated with the latter.

D. Spin current density

From Eq. (1), since $|\mathbf{j}_{\mathrm{s}} \times \mathbf{u}_P| = j_{\mathrm{s}} \sin(\vartheta_{\mathrm{Ge}})$, the time-dependent ISHE signal between the Ohmic contacts can be expressed as

$$\Delta V_{\mathrm{ISHE}}(t) = \gamma \ \langle j_{\mathrm{s}}(z,t) \rangle_z \ \rho \, d \ \sin(\vartheta_{\mathrm{Ge}}), \tag{2}$$

where ρ is the stripe resistivity and $\langle j_{\mathrm{s}}(z,t) \rangle_z$ is the spatial average along z of the spin current density $j_{\mathrm{s}}(z,t)$. Since the laser repetition rate is much higher than the PEM frequency, the demodulated signal ΔV_{ISHE} is the time average of Eq. (2) [47]. Thus, the measured ΔV_{ISHE} depends on the time- and space-averaged value of $j_{\mathrm{s}}(z,t)$. This value should be found by solving the time-dependent continuity equation for the spin density. Anyway, it is possible to simplify the problem by noticing that the time average of $j_{\mathrm{s}}(z,t)$ equals the solution $j_{\mathrm{s}}(z)$ of the spin-continuity equation in the steady state:

$$\frac{\partial j_{\mathrm{s}}(z)}{\partial z} = -\frac{n_{\mathrm{s}}(z)}{\tau_{\mathrm{s}}} + P_0 \, \alpha \, \Phi_{\mathrm{ph}} \, e^{-\alpha z}, \tag{3}$$

with $j_{\mathrm{s}}(z) = -D_{\mathrm{e}} \, \partial n_{\mathrm{s}}/\partial z$, α being the absorption coefficient, and $D_{\mathrm{e}} \approx 12\,(15)\,\mathrm{cm}^2/\mathrm{s}$ being the diffusion coefficient for n- (p-) doped Ge [48,49]. Equation (3) can be solved by imposing the boundary conditions $j_{\mathrm{s}}(0) = 0$ and $j_{\mathrm{s}}(d_z) = 0$, which express the fact that spin cannot leak from the stripe at the Ge/air ($z = 0$) and Ge/SiO$_2$ ($z = d_z$) interfaces. The value of $j_{\mathrm{s}}^{\mathrm{av}} = \langle j_{\mathrm{s}}(z) \rangle_z$ results by averaging $j_{\mathrm{s}}(z)$ over the stripe height d_z. The averaged spin current density (normalized to the photon flux Φ_{ph}) arising from spins photoexcited from the HH, LH, and SO branches is independently plotted in Fig. 4(b), which also shows the total spin current density resulting from the sum of the three contributions.

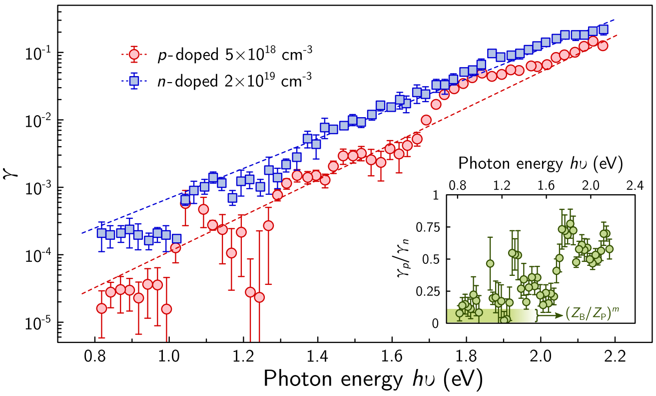

FIG. 5. Estimated spin-to-charge conversion parameter γ as a function of photon energy for n-doped (blue squares) and p-doped Ge (red circles). Dashed lines are guides for the eye. The inset shows the ratio γ_p/γ_n between the spin-to-charge conversion parameters for n- and p-doped Ge. In the inset, the band marks the expected ratio within an atomic picture, with m ranging between 2 and 4.

It should be noticed that holes have been neglected in these calculations due to their substantially lower spin lifetime [22,50]. Indeed, similar calculations accounting for hole spin currents return a negligible contribution to $j_{\mathrm{s}}^{\mathrm{av}}$. All the results reported in Fig. 4 assume n-type Ge, with the results for p-type Ge being only slightly different.

E. Spin-to-charge conversion

From Eq. (2) one can see that the measured signal ΔV_{ISHE} is proportional to $\gamma \ j_{\mathrm{s}}^{\mathrm{av}}$. Indeed, the change in sign in the total spin current density [Fig. 4(b)] nicely mimics what is observed in the experimental data [Fig. 2(d)]. However, the trends of ΔV_{ISHE} (measured) and $j_{\mathrm{s}}^{\mathrm{av}}$ (calculated) are quite different, thus pointing towards an energy dependence of γ, which can be estimated from Eq. (2) and is displayed in Fig. 5 for n- (blue squares) and p-doped Ge (red circles).

The value of γ for excitations around the direct gap for the n-doped sample ($\approx 2 \times 10^{-4}$) is in agreement with those already reported in the literature for n-doped Ge and related to L-point thermalized electrons [18,35]. The spin-to-charge conversion turns out to be much more efficient for hot electrons. Indeed, contrary to the calculated $j_{\mathrm{s}}^{\mathrm{av}}$, which decreases at high energy, the measured ΔV_{ISHE} increases. Since the ΔV_{ISHE} signals shown in Fig. 2(d) for n- and p-doped Ge are comparable, the difference between γ_n and γ_p balances the different resistivities for the two samples [see Eq. (2)].

It should be noticed that the experimental trend has roughly exponential growth (eye-guide lines in Fig. 5), and γ varies by

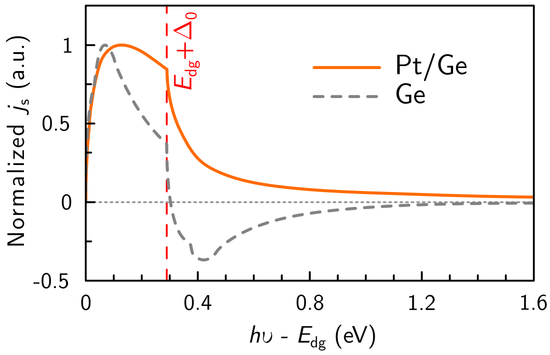

FIG. 6. Average spin current density inside a Ge stripe (dashed line) and spin current density injected into Pt in a Pt/Ge junction (solid line).

about 3 orders of magnitude for both samples in the explored photon energy range. Notably, a similar growth of γ has been observed in GaAs by Okamoto *et al.* [34]. Such a finding was explained by them as being due to the increase in the occupation probability of the L valley, in which spin-orbit coupling turned out to be much more efficient, with the electron kinetic energy.

The inset in Fig. 5 shows the ratio γ_p/γ_n between the spin-Hall angles for p- and n-doped samples. At photon energies up to $h\nu \approx 1.2$ eV we obtain $\gamma_p/\gamma_n \approx 0.1$, whereas at higher $h\nu$ the ratio increases up to 0.7. This behavior can be ascribed to a decreasing of the impurity-scattering cross section, occurring at high $h\nu$ values. In fact, no difference between p- and n-type Ge is expected when the spin-to-charge conversion is mediated by phonons. On the other hand, as discussed above, impurity scattering plays a relevant role at low photon energy (low kinetic energy). We note that spin-to-charge conversion due to impurity scattering is driven by the spin-orbit interaction (SOI) [32], which strongly depends on the atomic number Z of the scattering center. Assuming an atomistic picture with a $\propto Z^m$ behavior of the SOI scattering cross section, with m ranging between 2 and 4, we get $\gamma_p/\gamma_n \approx (Z_{\mathrm{B}}/Z_{\mathrm{P}})^m \approx$ 0.01–0.11, with B and P being the dopants of p- and n-type Ge, respectively. So the trend of the ratio γ_p/γ_n reflects the fact that up to 1.2 eV scattering is mostly due to impurities, while the contribution of the latter decreases with increasing photon energy. Consistently, at higher photon energy γ_p and γ_n approach the same value. Moreover, the paramount increase in γ when the photon energy (i.e., electrons' kinetic energy) is increased indicates that phonon scattering, more relevant at high kinetic energy, is a much more efficient process than impurity scattering as far as spin-to-charge conversion is concerned.

F. Pt/Ge junction

To prove the validity of the model, we test it on a different system. The high spin polarization achievable inside Ge motivates its exploitation as a spin generator and the study of spin transfer from the latter into other materials. In a previous work we performed such a study by analyzing a Pt/Ge Schottky junction [19,42]. In this case, thanks to the high SOI, ISHE mainly takes place in the metal, where spin-polarized carriers are injected from Ge. As shown in Ref. [19], the ISHE signal, proportional to the spin current density injected into Pt, does not show any sign reversal. Although at first glance this might appear to be in disagreement with the case of bulk Ge described above, by solving the drift-diffusion equation with the proper boundary conditions [51], our model does not predict any signal inversion, and the calculated j_{s} injected into Pt (Fig. 6) well reproduces the experimentally detected ISHE signal. This is a consequence of the fact that electrons diffusing from Ge into Pt mostly depolarize in the metal, at variance with the case discussed above where depolarization occurs in the semiconductor.

IV. CONCLUSION

We have exploited optical orientation to photogenerate spin-polarized carriers in highly doped Ge. The electric ISHE signal resulting from spin-dependent scattering has been detected as a function of the incident photon energy in the 0.7–2.2 eV range. A change in the sign of the measured signal for $h\nu \approx E_{\mathrm{dg}} + \Delta_0$ can be reproduced within a model describing momentum, energy, and spin relaxation. The inferred spin-Hall angle γ shows a variation of about 3 orders of magnitude in the investigated photon energy range for both n- and p-doped stripes. By comparing the γ values obtained for the two dopants for photon energies around the gap, our model confirms the role played by impurity scattering, as expected in an atomistic picture. Moreover, we have shown that, at higher photon energies, phonon scattering yields a more efficient spin-to-charge conversion than impurity scattering.

APPENDIX A: MOMENTUM SCATTERING

Following the Brooks-Herring approach [44] it is possible to evaluate the characteristic rate $(\tau_{\mathrm{m}}^{\mathrm{imp}})^{-1}$ of electron momentum scattering due to impurities as

$$\left(\tau_{\mathrm{m}}^{\mathrm{imp}}\right)^{-1} = \frac{N q^2}{16\pi\,\epsilon^2\sqrt{2\,m^*_{\mathrm{CB}}}}\left(\ln\left(1+\beta^2\right) - \frac{\beta^2}{1+\beta^2}\right)\varepsilon_{\mathrm{k}}{}^{-3/2}, \tag{A1}$$

where ϵ is the dielectric constant, q is the elementary charge, m^*_{CB} is the CB effective mass, N is the impurity concentration, and

$$\beta = \frac{8\,m^*_{\mathrm{CB}}\,\ell_{\mathrm{TF}}{}^2}{\hbar^2}\,\varepsilon_{\mathrm{k}}, \tag{A2}$$

where ℓ_{TF} is the Thomas-Fermi screening length. As discussed in Ref. [44], the scattering cross section decreases at high energies due to the reduction of the interaction between the electron and the scattering center.

Concerning the processes that involve phonon-scattering, absorption (a) and emission (e) of phonons should be considered. For an electron in a valley i the rate of scattering events transferring the electron to a valley j is [44]

$$\begin{aligned}\left(\tau_{ij}^{\mathrm{a(e)}}\right)^{-1} = {} & \frac{\pi\,M_j\,D_{ij}{}^2}{2\varrho\,\omega_{ij}}\,g\left(\varepsilon_{\mathrm{k}} - \Delta E_{ji} \underset{(-)}{+} \hbar\omega_{ij}\right)\\ & \times \left(n_{\mathrm{ph}} + 1/2 \underset{(+)}{-} 1/2\right),\end{aligned} \tag{A3}$$

where $M_j = 1$ for intravalley processes and M_j is equal to the degeneracy of the jth valley for intervalley ones, $\hbar\omega_{ij}$ is

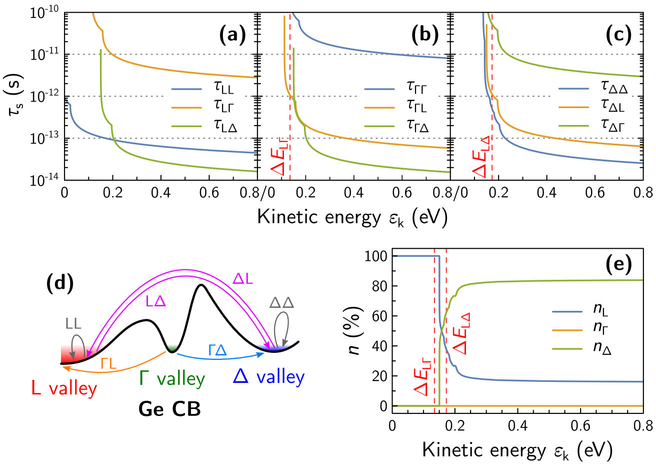

FIG. 7. Phonon momentum scattering time for electrons in (a) L, (b) Γ, and (c) Δ valleys. (d) Sketch of the leading phonon-scattering processes occurring in the Ge CB. (e) Valley occupation probability as a function of the kinetic energy.

the phonon energy (from Ref. [52]), D_{ij} is the deformation potential (from Ref. [52]), ϱ is the density of the material, $g(E)$ is the density of states, ΔE_{ji} is the energy separation between two valleys, and n_{ph} is the number of phonons given by Bose-Einstein statistics. In Figs. 7(a)–7(c) we report the scattering times for electrons in the L, Γ, and Δ valleys, identifying the processes in which electrons scatter in the same type of valley (τ_{ii}) or in a different one (τ_{ij}, $i \neq j$). The phonon-scattering processes leading the electron dynamics are sketched in Fig. 7(d).

It should be noted that L, Γ, and Δ scattering rates cannot be summed to find the total scattering rate because they are competitive processes (one electron cannot be in more than one valley at once). Thus, to get the effective scattering rate, it is necessary to find the valley distribution of electrons, which we discuss in Appendix B. To simplify the problem, from Figs. 7(a)–7(c) one can note that the scattering rate to a Γ valley is negligible due to its low density of states. On the contrary, scattering rates to L and Δ are of the same order of magnitude, with the latter being slightly larger.

APPENDIX B: VALLEY POPULATION

From the scattering rate it is possible to recover the probability $p(j|i)$ for an electron in a valley i to scatter in a valley j as

$$p(j|i) = \frac{\tau_{ij}{}^{-1}}{\sum_{k=0}^{2} \tau_{ik}{}^{-1}}, \tag{B1}$$

with $k = 0,1,2$ indicating the L, Γ and Δ valleys, respectively. To find the number n_i of electrons in the ith valley, we can impose the steady-state condition $n_i(t) = n_i(t + dt)$. The applicability of this assumption is ensured by the fact that both energy and spin relaxation require a large number of scattering events. Moreover, already at the first scattering event, the probability to scatter from Γ, where the spin population is generated, to L or Δ yields populations n_L and n_Δ close to the steady-state situation. Due to the negligible scattering probability to Γ the problem can be further simplified by assuming $n_\Gamma = 0$. We obtain

$$n_\Delta = \frac{1 - p(\mathrm{L}|\mathrm{L}) + p(\Delta|\mathrm{L})}{1 - p(\mathrm{L}|\mathrm{L}) + p(\Delta|\mathrm{L}) + p(\mathrm{L}|\Delta)}, \tag{B2a}$$

$$n_L = 1 - n_\Delta, \tag{B2b}$$

which are plotted in Fig. 7(e). At this point, it is possible to correctly take into account these competitive processes to get the overall phonon-scattering rate:

$$\tau_{\mathrm{ph}}{}^{-1} = \sum_{i=0}^{2} n_i \sum_{k=0}^{2} p(k|i)\, \tau_{ik}{}^{-1}, \tag{B3}$$

which gives τ_{ph} [red line in Fig. 3(a)].

APPENDIX C: SPIN-RELAXATION TIMES

Once the momentum scattering rate is known, it is possible to derive the kinetic energy dependence of the spin-scattering rate from the Yafet-Elliot relation as [45]

$$\tau_{\mathrm{s}}{}^{-1} = \left(\frac{\Delta_0}{E_{\mathrm{dg}} + \Delta_0} \frac{\varepsilon_{\mathrm{k}}}{E_{\mathrm{dg}}} \right)^2 \tau_{\mathrm{m}}{}^{-1}, \tag{C1}$$

which gives $\tau_{\mathrm{s}} \propto \tau_{\mathrm{m}}/\varepsilon_{\mathrm{k}}{}^2$, as reported in the text. When ε_{k} approaches zero, due to the finite value of τ_{m}, τ_{s} diverges. The spin lifetime for thermalized electrons is not a key term in our model. Anyway, to better describe this parameter we exploit the models of Refs. [53,54], also taking into account the Bir-Aronov-Pikus (BAP) mechanism for p-doped Ge [10,55]. Indeed, exchange interaction can mediate spin transfer from electrons to holes, where spins quickly depolarize [55]. BAP scattering rate can be expressed as [10,55]

$$\left(\tau_{\mathrm{BAP}}^{\mathrm{s}}\right)^{-1} = \frac{2}{\tau_{\mathrm{BAP}}^{\mathrm{s}0}} \frac{v_{\mathrm{F}}}{v_{\mathrm{B}}} \frac{\varepsilon_{\mathrm{k}}}{E_{\mathrm{F}}} N_{\mathrm{a}} a_{\mathrm{B}}{}^3, \tag{C2}$$

where v_{F} and E_{F} are hole Fermi velocity and energy, respectively, N_{a} is the acceptor number, a_{B} and v_{B} are the Bohr radius and velocity, respectively, and $\tau_{\mathrm{BAP}}^{\mathrm{s}0}$ [55] is

$$\left(\tau_{\mathrm{BAP}}^{\mathrm{s}0}\right)^{-1} = \frac{3\pi}{64\,\hbar} \frac{\Delta E_{\mathrm{SR}}{}^2}{E_{\mathrm{B}}}, \tag{C3}$$

in which ΔE_{SR} is the short-range exchange splitting of the exciton ground state and E_{B} is the Bohr energy of the exciton. We estimate a ratio $v_{\mathrm{F}}/v_{\mathrm{B}} \approx 1.3$, $a_{\mathrm{B}} \approx 6.4$ nm, $\Delta E_{\mathrm{SR}} \approx 58\,\mu$eV [56], $E_{\mathrm{B}} \approx 6.9$ meV, and $E_{\mathrm{F}} \approx 31$ meV. Although BAP scattering is the leading term for a thermalized electron population in p-doped Ge, as energy slightly increases, it rapidly becomes negligible compared to the other scattering processes.

[1] D. D. Awschalom and M. E. Flatté, Nat. Phys. **3**, 153 (2007).
[2] I. Žutić, J. Fabian, and S. D. Sarma, Rev. Mod. Phys. **76**, 323 (2004).
[3] J. Fabian, A. Matos-Abiague, C. Ertler, P. Stano, and I. Žutić, Acta Phys. Slovaca **57**, 565 (2007).
[4] J. Xia, W. Ge, and K. Chang, *Semiconductor Spintronics* (World Scientific, Singapore, 2012).
[5] Y. D. Park, Science **295**, 651 (2002).
[6] D. L. Smith and R. N. Silver, Phys. Rev. B **64**, 045323 (2001).
[7] F. Rortais, C. Vergnaud, A. Marty, L. Vila, J.-P. Attané, J. Widiez, C. Zucchetti, F. Bottegoni, H. Jaffrès, J.-M. George, and M. Jamet, Appl. Phys. Lett. **111**, 182401 (2017).
[8] R. Takahashi, M. Matsuo, M. Ono, K. Harii, H. Chudo, S. Okayasu, J. Ieda, S. Takahashi, S. Maekawa, and E. Saitoh, Nat. Phys. **12**, 52 (2015).
[9] G. Lampel, Phys. Rev. Lett. **20**, 491 (1968).
[10] F. Meier and B. Zakharchenya, in *Optical Orientation*, Modern Problems in Condensed Matter Sciences Vol. 8 (North-Holland, Amsterdam, 1984), pp. 15–129.
[11] D. T. Pierce and F. Meier, Phys. Rev. B **13**, 5484 (1976).
[12] A. Ferrari, F. Bottegoni, G. Isella, S. Cecchi, and F. Ciccacci, Phys. Rev. B **88**, 115209 (2013).
[13] F. Bottegoni, G. Isella, S. Cecchi, and F. Ciccacci, Appl. Phys. Lett. **98**, 242107 (2011).
[14] Y. K. Kato, R. C. Myers, A. C. Gossard, and D. D. Awschalom, Science **306**, 1910 (2004).
[15] K. Ando, M. Morikawa, T. Trypiniotis, Y. Fujikawa, C. H. W. Barnes, and E. Saitoh, J. Appl. Phys. **107**, 113902 (2010).
[16] K. Ando, M. Morikawa, T. Trypiniotis, Y. Fujikawa, C. H. W. Barnes, and E. Saitoh, Appl. Phys. Lett. **96**, 082502 (2010).
[17] F. Bottegoni, A. Ferrari, G. Isella, M. Finazzi, and F. Ciccacci, Phys. Rev. B **88**, 121201 (2013).
[18] F. Bottegoni, C. Zucchetti, S. D. Conte, J. Frigerio, E. Carpene, C. Vergnaud, M. Jamet, G. Isella, F. Ciccacci, G. Cerullo, and M. Finazzi, Phys. Rev. Lett. **118**, 167402 (2017).
[19] F. Bottegoni, A. Ferrari, S. Cecchi, M. Finazzi, F. Ciccacci, and G. Isella, Appl. Phys. Lett. **102**, 152411 (2013).
[20] F. Bottegoni, M. Celebrano, M. Bollani, P. Biagioni, G. Isella, F. Ciccacci, and M. Finazzi, Nat. Mater. **13**, 790 (2014).
[21] C. Zucchetti, F. Bottegoni, C. Vergnaud, F. Ciccacci, G. Isella, L. Ghirardini, M. Celebrano, F. Rortais, A. Ferrari, A. Marty, M. Finazzi, and M. Jamet, Phys. Rev. B **96**, 014403 (2017).
[22] F. Bottegoni, C. Zucchetti, F. Ciccacci, M. Finazzi, and G. Isella, Appl. Phys. Lett. **110**, 042403 (2017).
[23] J. Rioux and J. E. Sipe, Phys. Rev. B **81**, 155215 (2010).
[24] J. L. Cheng, J. Rioux, J. Fabian, and J. E. Sipe, Phys. Rev. B **83**, 165211 (2011).
[25] H. Dery, P. Dalal, Ł. Cywiński, and L. J. Sham, Nature (London) **447**, 573 (2007).
[26] M. I. Dyakonov and V. I. Perel, Zh. Eksp. Teor. Fiz. **60**, 1954 (1971) [Sov. Phys. JETP **33**, 1053 (1971)].
[27] F. Bottegoni, H.-J. Drouhin, J.-E. Wegrowe, and G. Fishman, J. Appl. Phys. **111**, 07C305 (2012).
[28] F. Bottegoni, H.-J. Drouhin, G. Fishman, and J.-E. Wegrowe, Phys. Rev. B **85**, 235313 (2012).
[29] M. Hochberg and T. Baehr-Jones, Nat. Photonics **4**, 492 (2010).
[30] M. J. Süess, R. Geiger, R. A. Minamisawa, G. Schiefler, J. Frigerio, D. Chrastina, G. Isella, R. Spolenak, J. Faist, and H. Sigg, Nat. Photonics **7**, 466 (2013).
[31] M. I. Dyakonov and A. Khaetskii, in *Spin Physics in Semiconductors* (Springer-Verlag, Berlin, Heidelberg, 2008), pp. 211–243.
[32] H.-A. Engel, B. I. Halperin, and E. I. Rashba, Phys. Rev. Lett. **95**, 166605 (2005).
[33] K. Ando and E. Saitoh, Nat. Commun. **3**, 629 (2012).
[34] N. Okamoto, H. Kurebayashi, T. Trypiniotis, I. Farrer, D. A. Ritchie, E. Saitoh, J. Sinova, J. Mašek, T. Jungwirth, and C. H. W. Barnes, Nat. Mater. **13**, 932 (2014).
[35] J.-C. Rojas-Sánchez, M. Cubukcu, A. Jain, C. Vergnaud, C. Portemont, C. Ducruet, A. Barski, A. Marty, L. Vila, J.-P. Attané, E. Augendre, G. Desfonds, S. Gambarelli, H. Jaffrès, J.-M. George, and M. Jamet, Phys. Rev. B **88**, 064403 (2013).
[36] F. Rortais, S. Oyarzún, F. Bottegoni, J. C. Rojas-Sánchez, P. Laczkowski, A. Ferrari, C. Vergnaud, C. Ducruet, C. Beigné, N. Reyren, A. Marty, J. P. Attané, L. Vila, S. Gambarelli, J. Widiez, F. Ciccacci, H. Jaffrès, J. M. George, and M. Jamet, J. Phys. Condens. Matter **28**, 165801 (2016).
[37] F. Pezzoli, L. Qing, A. Giorgioni, G. Isella, E. Grilli, M. Guzzi, and H. Dery, Phys. Rev. B **88**, 045204 (2013).
[38] A. Giorgioni, E. Vitiello, E. Grilli, M. Guzzi, and F. Pezzoli, Appl. Phys. Lett. **105**, 152404 (2014).
[39] V. Reboud, A. Gassenq, K. Guilloy, G. O. Dias, J. M. Escalante, S. Tardif, N. Pauc, J. M. Hartmann, J. Widiez, E. Gomez, E. B. Amalric, D. Fowler, D. Rouchon, I. Duchemin, Y. M. Niquet, F. Rieutord, J. Faist, R. Geiger, T. Zabel, E. Marin, H. Sigg, A. Chelnokov, and V. Calvo, Proc. SPIE **9752**, 97520F (2016).
[40] SuperK Extreme EXW-12, NKT Photonics. Note that we do not exploit the temporal structure of the laser source; that is, our results are time averaged, as would be obtained with a continuous-wave laser.
[41] M. Savoini, F. Ciccacci, L. Duò, and M. Finazzi, Rev. Sci. Instrum. **82**, 023709 (2011).
[42] F. Bottegoni, A. Ferrari, F. Rortais, C. Vergnaud, A. Marty, G. Isella, M. Finazzi, M. Jamet, and F. Ciccacci, Phys. Rev. B **92**, 214403 (2015).
[43] S. Jain and D. Roulston, Solid State Electron. **34**, 453 (1991).
[44] M. Lundstrom, *Fundamentals of Carrier Transport*, 2nd ed. (Cambridge University Press, Cambridge, 2009).
[45] C. Guite and V. Venkataraman, Appl. Phys. Lett. **101**, 252404 (2012).
[46] S. K. Khamari, V. K. Dixit, and S. M. Oak, J. Phys. D **44**, 265104 (2011).
[47] The electric voltage measured between the two Ohmic pads and the one generated at the edges of the lighted area are related by a geometrical parameter expressed in Ref. [42]. Here, we do not find any difference between the two electric signals, with the geometrical parameter being ≈ 1.
[48] V. I. Fistul, M. I. Iglitsyn, and E. M. Omelyanovskii, Sov. Phys. Solid State **4**, 784 (1962).
[49] S. S. Li and F. Lindholm, Proc. IEEE **56**, 1256 (1968).
[50] I. Žutić, J. Fabian, and S. D. Sarma, Phys. Rev. B **64**, 121201 (2001).
[51] G. Isella, F. Bottegoni, A. Ferrari, M. Finazzi, and F. Ciccacci, Appl. Phys. Lett. **106**, 232402 (2015).
[52] M. Fischetti, IEEE Trans. Electron Devices **38**, 634 (1991).
[53] P. Li, Y. Song, and H. Dery, Phys. Rev. B **86**, 085202 (2012).
[54] T. Yu and M. W. Wu, J. Phys. Condens. Matter **27**, 255001 (2015).
[55] M. Wu, J. Jiang, and M. Weng, Phys. Rep. **493**, 61 (2010).
[56] H. Fu, L.-W. Wang, and A. Zunger, Phys. Rev. B **59**, 5568 (1999).